*Korean J. Chem. Eng.*, 35(1), 257-262 (2018)
DOI: 10.1007/s11814-017-0247-2

pISSN: 0256-1115
eISSN: 1975-7220

# Manganese oxide with different composition and morphology as electrocatalyst for oxygen evolution reaction

**Hwansu Sim*,‡, Jooyoung Lee*,‡, Taekyung Yu**,†, and Byungkwon Lim*,†**

*School of Advanced Materials Science and Engineering, Sungkyunkwan University (SKKU), Suwon 16419, Korea
**Department of Chemical Engineering, Kyung Hee University, Yongin 17104, Korea
(*Received 7 July 2017 • accepted 10 September 2017*)

**Abstract**−Electrochemical activity and stability depend on the composition and morphology of nanocrystals. $Mn_3O_4$ nanoplates, $Mn_2O_3$ nanoplates, and porous $Mn_2O_3$ nanoplates were synthesized by heat treatment of Mn-glycolate nanoplates prepared by the wet-chemical method. In this research, the morphology and composition of the nanoplates could be easily controlled by varying the annealing temperature. The synthesized porous $Mn_2O_3$ nanoplates exhibited better electrocatalytic activities compared with $Mn_3O_4$ and $Mn_2O_3$ nanoplates, as similar as commercial $IrO_2$ catalyst.

Keywords: Manganese Oxides, Composition, Porous Structure, Oxygen Evolution Reaction, Stability

## INTRODUCTION

With the rising cost of fossil fuels and the environmental hazards, various energy industries using hydrogen have become more important in the 21st century, and intrusion into hydrogen production has also been amplified [1-3]. The oxygen evolution reaction (OER), which is a half electrochemical reaction of the water splitting that decomposes water to generate oxygen, is known as one of the causes of reducing the overall reaction rate due to its low efficiency compared to the hydrogen generation reaction [4-6]. To overcome this problem, researches to increase the efficiency of the OER by using nanoparticles as catalyst have been carried out steadily [7-9]. In general, OER uses noble metals and noble metal oxides such as $IrO_2$ and $RuO_2$ as catalysts [10-12]. However, their high price limits the efficiency of the OER. Recently, the use of low cost transition metal oxide as a new OER catalyst has been studied extensively, but it has limitations due to its high over potential [13-16].

Manganese oxides, one of the transition metal oxides, have been attractive as an electrochemical catalyst due to their low cost and various crystal structures with various oxidation numbers [17-20]. In particular, manganese oxide nanostructures are expected to be candidate materials that can replace existing noble metal oxide catalysts in the OER because of the increase of reaction efficiency due to wide electrochemical surface area [21-23]. However, as the size of the nanoparticles becomes smaller, there is a problem that the catalyst stability greatly decreases during the reaction [24]. Therefore, it is necessary to solve the stability problem in order to use the manganese oxide nanostructure as an actual OER catalyst.

In general, the catalytic property of metal oxide can be modulated by controlling their size, crystallinity, morphology, and crystal structure [25-27]. Hollow nanostructures which have nm-sized pores can have high stability against reaction as well as good catalytic activity because they have a large surface area per weight but have many atoms per particle. In this research, we developed a new method to control the crystal structure and morphology of manganese oxide nanocrystals, including $Mn_3O_4$ nanoplates, $Mn_2O_3$ nanoplates, and porous $Mn_2O_3$ nanoplates, and compared their electrocatalytic activity and stability as OER catalysts. Morphology and composition controlled manganese oxide nanoplates were synthesized by the following two-step procedure. First, Mn-glycolate nano-

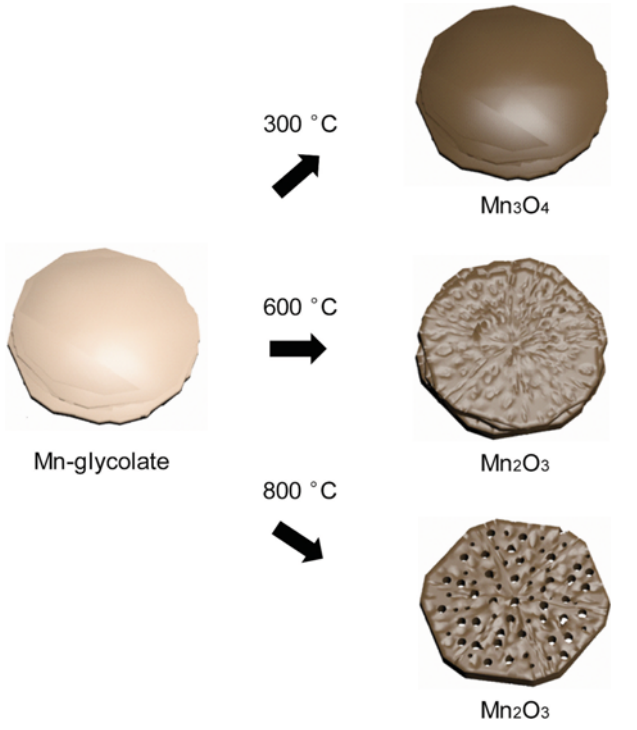


**Scheme 1. Schematic illustration of reaction pathways for the synthesis of the $Mn_3O_4$, $Mn_2O_3$, and porous $Mn_2O_3$ nanoplates.**

†To whom correspondence should be addressed.
E-mail: tkyu@khu.ac.kr, blim@skku.edu
‡These authors contributed equally to this work.

plates were prepared by wet-chemical method. Next, manganese oxide nanoplates were formed by heat treatment of Mn-glycolate nanoplates. We could easily control the morphology and composition of the nanoplates just by varying the annealing temperature (Scheme 1). The synthesized porous $Mn_2O_3$ nanoplates exhibited better electrocatalytic activities compared with $Mn_3O_4$ and $Mn_2O_3$ nanoplates, as similar as commercial $IrO_2$ catalyst.

## EXPERIMENTAL SECTION

### 1. Materials

Manganese(II) nitrate tetrahydrate ($Mn(NO_3)_2{\cdot}4H_2O$), ethylene glycol, and oleylamine were purchased from Aldrich, Samchun, and Acros, respectively. They were used without further purification.

### 2. Synthesis of Manganese Oxide Nanoplates

0.25 mmol of manganese(II) nitrate tetrahydrate ($Mn(NO_3)_2{\cdot}4H_2O$, Sigma Aldrich) was dissolved in 9 mL of ethylene glycol (Samchun). 1 mL of oleylamine (Across) was injected into the ethylene glycol solution. The mixture solution was then heated to 150 °C and aged at the same temperature for 4 h without stirring. The product was washed with ethanol several times to remove excess reagents and then dried in oven at 80 °C for overnight. The products were placed in tube furnace and slowly heated to appropriate temperature (300, 600, and 800 °C) in air. To obtain $Mn_2O_3$ and $Mn_3O_4$ nanoplates, the products were annealed at 300 and 600 °C for 5 h, respectively. Porous $Mn_2O_3$ nanoplates were obtained by annealing at 800 °C for 7 h. The final products were cooled to room temperature.

### 3. Characterization

The scanning electron microscopy (SEM) image was obtained by SUPRA 55VP (Carl Zeiss). The transmission electron microscopy (TEM) image was captured by JEM-2100F microscopy operating at 200 kV. The powder X-ray diffraction (XRD) patterns were recorded by D8-Advances (Bruker AXS) diffractometry equipped with a rotating anode and a Cu Ka radiation source ($\lambda$=0.15418 nm). X-ray photoelectron spectroscopy (XPS) spectra were obtained by ECSA2000 (VG Microtech). Fourier transform infrared spectroscopy (FT-IR) spectra were obtained by Bruker IFS-66/S. Thermogravimetric analysis (TGA) curves were obtained by Discovery TGA (TA Instruments).

### 4. Electrochemical Measurements

Electrochemical measurements were tested by three-electrode system in 0.1 M KOH solution. Hg/HgO (in 1 M NaOH solution) and Pt wire were used as reference electrodes and counter electrodes, respectively. The electrocatalyst inks were prepared by mixing a sample, polyvinylidene fluoride (PVDF), and ketjen black (weight ratio was 7 : 2 : 1) in *N*-methyl-2-pyrrolidone (NMP). The catalyst inks were loaded onto Ni foam. The Ni foam loaded inks were dried in oven at 80 °C for overnight. The cyclic voltammetry (CV) curves were measured by using WBCS-3000 (WonATech) in the potential range between 1.2 and 2.0 V (vs. RHE) at a scan rate of 1 mV/s.

## RESULTS AND DISCUSSION

Mn-glycolate nanoplates were prepared by slightly modifying a

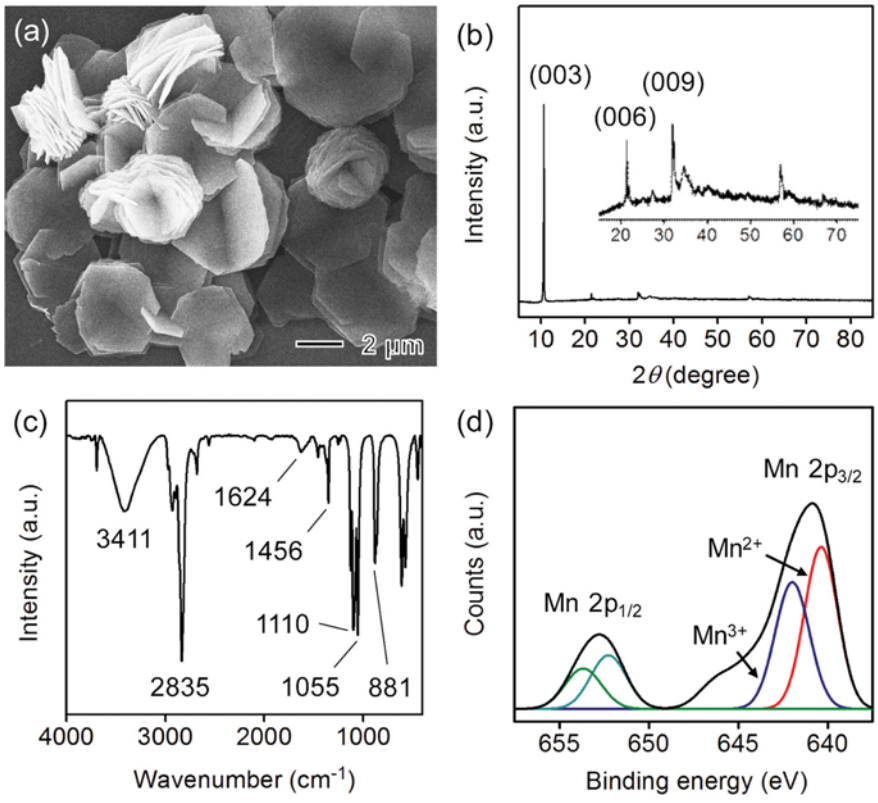


**Fig. 1. (a) SEM image, (b) XRD patterns, (c) FT-IR spectrum, and (d) XPS Mn 2p core spectrum of Mn-glycolate nanoplates.**

previously reported method [28-31]. SEM image shows the formation of nanoplates with sizes of around 1-5 μm (Fig. 1(a)). The XRD patterns of the nanoplates indicate the presence of diffraction peaks at $2\theta$ values of 10.7, 21.5, and 32.0°, which are well matched with previous reported result of (003), (006), and (009) planes of the brucite-like Mn-glycolate structures (Fig. 1(b)) [28,29]. We obtained FT-IR spectrum to determine the structure of the organic chemical present on the surface of the nanoplates. A strong absorption band at 2,500-3,000 $cm^{-1}$ is assigned to C-H stretching band and peaks at 881, 1,055, 1,110, and 1,456 $cm^{-1}$ can be indexed to Mn-O, C-C, C-O, and $CH_2$ bonds, respectively, indicating that all FT-IR peaks are well matched with previous literature values (Fig. 1(c)) [28,29]. In addition, the Mn XPS 2p core level spectrum shown in Fig. 1(d) could be divided two sets of 2p peaks. One set included a Mn $2p_{3/2}$ peak at 640.4 eV and Mn $2p_{1/2}$ at 652.3 eV, respectively, corresponding to $Mn^{2+}$. The other set had a $Mn2p_{3/2}$ peak at 642.0 eV and the $Mn2p_{1/2}$ peak at 653.7 eV, which can represent $Mn^{3+}$ [32,33]. This observation demonstrates that the synthesized Mn-glycolate is composed of bivalent and trivalent Mn.

$Mn_3O_4$ and $Mn_2O_3$ nanoplates were synthesized by the annealing process using the Mn-glycolate nanoplates as a starting material in an air atmosphere. The XRD patterns of the sample obtained by the annealing process at 300 °C for 5 h show the presence of diffraction peaks at peaks at $2\theta$ values of 18.1, 28.8, 31.6 and 36.8°, which can be indexed to (101), (112), (103), and (211) planes of spinel structure of $Mn_3O_4$, respectively (JCPDs card No. 24-0734, Fig. 2). The size of the $Mn_3O_4$ nanoplates was 1-5 μm, similar to that of the Mn-glycolate nanoplates (Fig. 3(a)). The surface of the

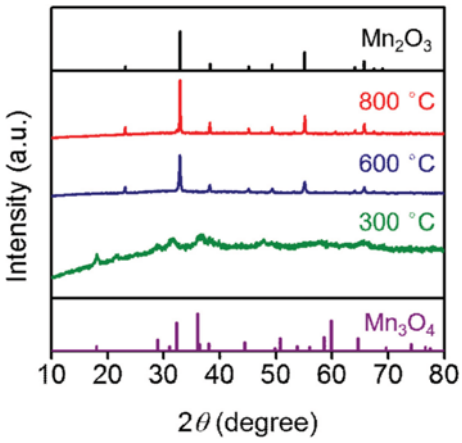


**Fig. 2. XRD patterns of manganese oxides obtained by the annealing process at 300, 600, and 800 °C.**

nanoplates was flat without cracks, indicating the formation of dense $Mn_3O_4$ nanoplates (Fig. 3(b)). When we increased the annealing temperature of 600 °C, the crystal structure of the nanoplates changed dramatically from $Mn_3O_4$ to $Mn_2O_3$ while keeping their morphology. The XRD patterns of the sample synthesized under annealing temperature of 600 °C showed diffraction peaks at $2\theta$ values of 23.1, 32.9, 38.2 and 55.1°, which can be well indexed to (211), (222), (400), and (440) planes of cubic-bixbyite structure of $Mn_2O_3$, respectively (JCPDs card No. 73-1826, Fig. 2). The overall morphology of $Mn_2O_3$ nanoplates was similar to that of $Mn_3O_4$,

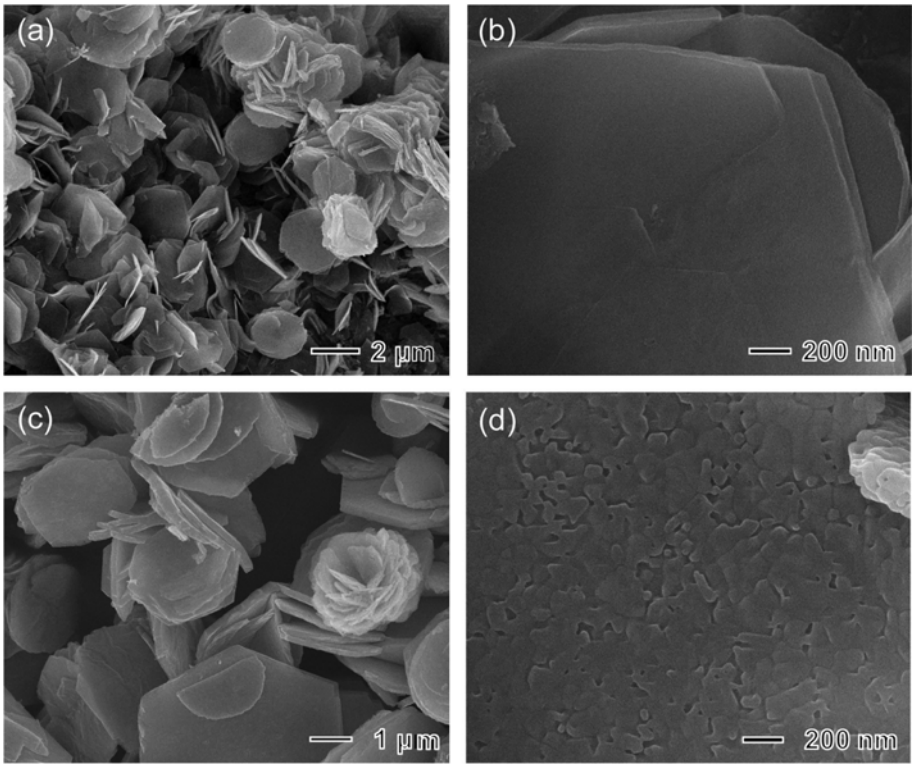


**Fig. 3. (a), (b) SEM images of $Mn_3O_4$ nanoplates obtained at an annealing temperature of 300 °C. (c), (d) SEM images of $Mn_2O_3$ nanoplates obtained at an annealing temperature of 600 °C.**

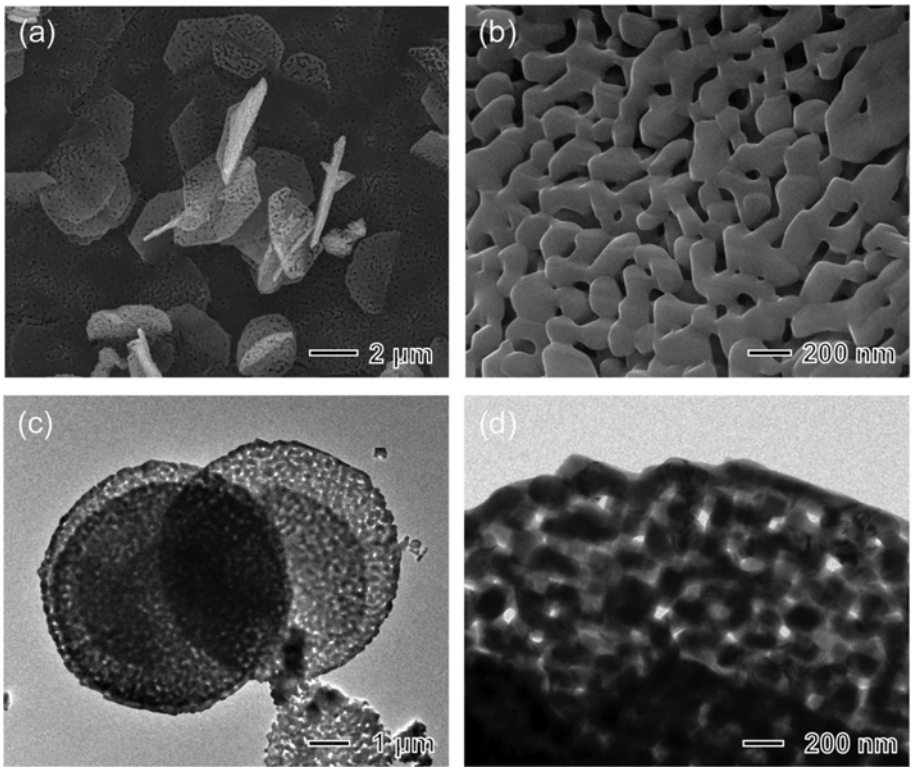


**Fig. 4. (a), (b) SEM and (c), (d) TEM images of porous $Mn_2O_3$ nanoplates obtained at an annealing temperature of 800 °C.**

but the surface of the nanoplates was not smooth and very rough (Fig. 3(c) and (d)). We believe that the rough and cracked surface of the nanoplates originated from the large volume change caused by the oxygen and organic molecules escaping during the annealing process. The initial weight loss of 5% under 220 °C was due to removing absorbed water molecules. The decomposition of organic molecules caused weight loss of 30% at 220-300 °C. The weight slightly decreased above 230 °C (Fig. S1).

Generally, soft or hard template methods are used to produce porous materials with a pore size of nm-scale [34,35]. In this case, an additional process was required to remove the template from the product. We could easily fabricate porous metal oxide nanoplates using the volume change that occurs by the composition change during the annealing process. Porous $Mn_2O_3$ nanoplates were synthesized by heating Mn-glycolate nanoplates at high annealing temperature of 800 °C for 7 h. SEM image of the sample shows the formation of porous nanoplates (Fig. 4(a)). High-resolution SEM and TEM analyses showed that nanoplate having approximately 100 nm-sized pores consists of a 3D hollow network structure aligned by angled nanoparticles with sizes of around 100 nm (Fig. 4(b) to (d)). It is presumed that Mn-glycolate is converted into oxide at high temperature, and the space remaining as the organic molecule evaporates and volume contraction due to recrystallization makes a porous structure. In addition, we also found that the crystallinity of the porous $Mn_2O_3$ nanoplate was improved compared with $Mn_2O_3$ nanoplates prepared at 600 °C by the increase of the intensity of the XRD peaks (Fig. 2). It means the crystal grain size of porous $Mn_2O_3$ is bigger than that of $Mn_2O_3$. We believe that it makes high conductivity and good electrochemical performance [36].

We evaluated the catalytic properties for the OER using the $Mn_3O_4$ nanoplates, $Mn_2O_3$ nanoplates, porous $Mn_2O_3$ nanoplates, and commercial $IrO_2$ nanoparticles (Fig. S2) as catalysts. Fig. 5(a) shows OER polarization curves of four catalysts performed at room temperature in a 0.1 M KOH solution at a scan rate of 1 mV/s from a positive to negative potential direction on a reversible hydrogen electrode (RHE) scale. Overpotential values of the catalysts at the current density of 10 mV/cm$^2$ were 500 mV for $Mn_3O_4$ nanoplates, 460 mV for dense $Mn_2O_3$ nanoplates, 420 mV for porous $Mn_2O_3$ nanoplates, and 460 mV for commercial $IrO_2$ nanoparticles, respectively (Fig. 5(b)). Dense and porous $Mn_2O_3$ nanoplates exhibited low overpotential values compared with $Mn_3O_4$ nanoplates, indicating that crystal structure of the manganese oxide is one of the important factors in the electrochemical reaction. Through electrochemical oxidation of $Mn_2O_3$, an oxygen vacancy would be formed in the structure, hydroxide ions in the electrolyte are adsorbed in this vacancy, and the reaction of desorbing oxygen and water molecules through electrochemical reaction proceeds [37]. The crystal structure of $Mn_2O_3$ has two types of edge sharing groups, including long Mn(III)-O bonds and short O-O bonds compared to $Mn_3O_4$. Relatively long and weak Mn(III)-O bonds promote water oxidation and short O-O bonds can promote the production of $O_2$ [37]. In addition, $Mn_2O_3$ has higher conductivity than $Mn_3O_4$ and exhibits higher characteristics [38]. We believe that these two characteristics of $Mn_2O_3$ lead to higher electrochemical properties compared with $Mn_3O_4$ nanoplates. In the $Mn_2O_3$ nanoplates, the porous $Mn_2O_3$ nanoplates have a higher surface area (16.5 mF/cm$^2$) than $Mn_2O_3$ nanoplates (1.1 mF/cm$^2$). As a result, the porous

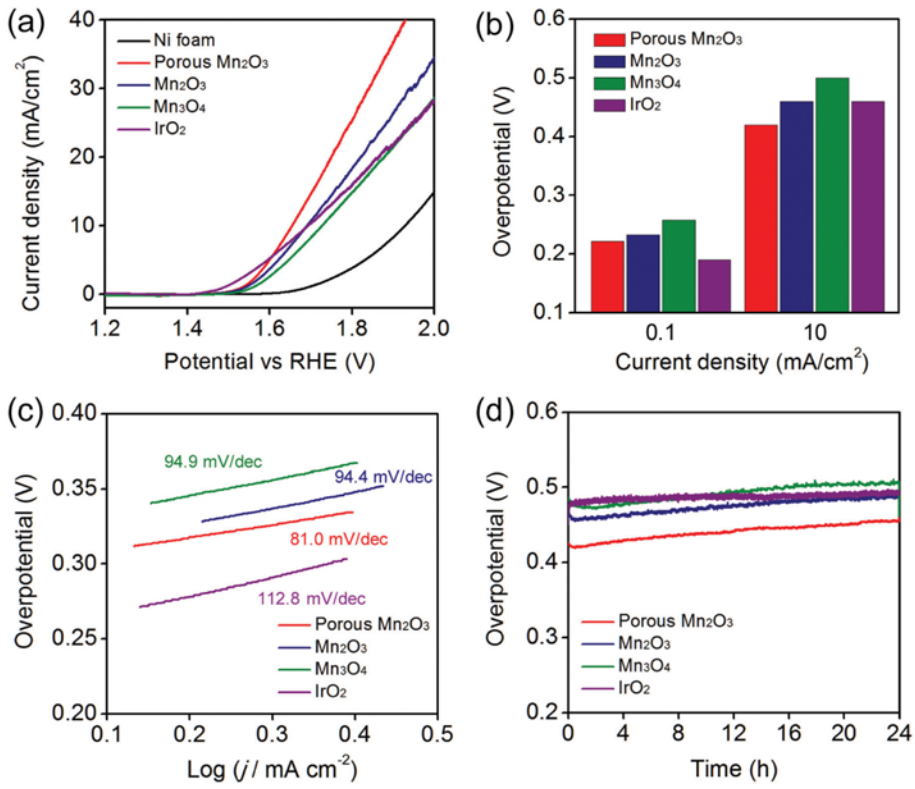


**Fig. 5. (a) OER polarization curves measured in 0.1 M KOH at room temperature at a scan rate of 1 mV/s from positive to negative potential without *iR* compensation. (b) The corresponding overpotentials of different electrocatalysts at current density of 0.1 and 10 mA/cm$^2$. (c) Tafel plots of different electrocatalysts. (d) Chronopotentiometry curves of different electrocatalysts at a constant current density of 10 mA/cm$^2$ for 24 h.**

ones had a lower overpotential than dense ones due to the high electrochemical surface area. As a part of efforts to obtain a better understanding of the electrochemical properties of the catalysts, the Tafel slope of each catalyst was calculated (Fig. 5(c)). The linear portions of the Tafel plots are fitted to the Tafel equation ($(\eta = b \log j/j_o)$, where $\eta$ is the overpotential, b is Tafel slope, j is the current density, and $j_o$ is exchange current density). The Tafel slope is an index revealing the relationship between the rate of oxygen evolution reaction with the change in the potential applied to the catalyst. The lower the value of the Tafel slope, the higher the sensitivity of the OER to the electric potential applied to the electrocatalyst, indicating that the efficiency is higher. The Tafel slopes were 94.9 mV/des for $Mn_3O_4$ nanoplates, 94.4 mV/dec for dense $Mn_2O_3$ nanoplates, 81.0 mV/dec for porous $Mn_2O_3$ nanoplates, and 112.8 mV/dec for commercial $IrO_2$ nanoparticles, respectively. As a result of the above overpotential measurement and Tafel slope, we conclude that the porous $Mn_2O_3$ nanoplates have better electrocatalytic activity in the OER than the commercial $IrO_2$ nanoparticles. In addition, we found that the overpotential value of the porous $Mn_2O_3$ nanoplates increased slightly after 24 hours of OER, but it did not increase much compared to the $Mn_3O_4$ and dense $Mn_2O_3$ nanoplates (Fig. 5(d)). SEM image of the porous $Mn_2O_3$ nanoplates after 24 h of OER shows that nanoplates maintained their porous structure (Fig. S4). Therefore, it was found that the porous structure did not significantly affect the stability [39].

## CONCLUSIONS

We have demonstrated a new method to control the crystal structure and morphology of manganese oxide nanocrystals, including $Mn_3O_4$ nanoplates, $Mn_2O_3$ nanoplates, and porous $Mn_2O_3$ nanoplates, and their electrocatalytic activity and stability in the OER. High annealing temperature of Mn-glycolate nanoplates led to the formation of porous $Mn_2O_3$ nanoplates and they exhibited good catalytic activity and stability, as similar as commercial $IrO_2$ catalyst. Just by changing the annealing temperature, we could control the composition and morphology of the nanocrystals, from $Mn_3O_4$ nanoplates to $Mn_2O_3$ nanoplates and porous $Mn_2O_3$ nanoplates. We expect that this approach could be extended to other transition metal oxide nanocrystals to improve their physical and chemical properties.

## ACKNOWLEDGEMENTS

This work was supported by the Basic Science Research Program (No. 2015R1A2A2A01006325) through the National Research Foundation (NRF) of Korea, funded by the Ministry of Science, ICT & Future Planning.

## SUPPORTING INFORMATION

Additional information as noted in the text. This information is

available via the Internet at http://www.springer.com/chemistry/journal/11814.

## REFERENCES


1. J. A. Turner, *Science*, **305**, 972 (2004).
2. N. Armaroli and V. Balzani, *ChemSusChem*, **4**, 21 (2011).
3. A. L. Goff, V. Artero, B. Jousselme, P. D. Tran, N. Guillet, R. Métayé, A. Fihri, S. Palacin and M. Fontecave, *Science*, **326**, 1384 (2009).
4. H. Dau and I. Zaharieva, *Acc. Chem. Res.*, **42**, 1861 (2009).
5. L. Duan, L. Tong, Y. Xu and L. Sun, *Energy Environ. Sci.*, **4**, 3296 (2011).
6. R. Cao, W. Lai and P. Du, *Energy Environ. Sci.*, **5**, 8134 (2012).
7. T. Reier, M. Oezaslan and P. Strasser, *ACS Catal.*, **2**, 1765 (2012).
8. Y. Li, H. Wang, L. Xie, Y. Liang, G. Hong and H. Dai, *J. Am. Chem. Soc.*, **133**, 7296 (2011).
9. H. G. S. Casalongue, M. L. Ng, S. Kaya, D. Friebel, H. Ogasawara and A. Nilsson, *Angew. Chem. Int. Ed.*, **53**, 7169 (2014).
10. T. Nakagawa, N. S. Bjorge and R. W. Murray, *J. Am. Chem. Soc.*, **131**, 15578 (2009).
11. T. Nakagawa, C. A. Beasley and R. W. Murray, *J. Phys. Chem. C*, **113**, 12958 (2009).
12. Y. Lee, J. Suntivich, K. J. May, E. E. Perry and Y. Shao-Horn, *J. Phys. Chem. Lett.*, **3**, 399 (2012).
13. J. Suntivich, K. J. May, H. A. Gasteiger, J. B. Goodenough and Y. Shao-Horn, *Science*, **334**, 1383 (2011).
14. M. W. Louie and A. T. Bell, *J. Am. Chem. Soc.*, **135**, 12329 (2013).
15. R. D. L. Smith, M. S. Prévot, R. D. Fagan, Z. Zhang, P. A. Sedach, M. K. J. Siu, S. Trudel and C. P. Berlinguette, *Science*, **340**, 60 (2013).
16. M. S. Burke, M. G. Kast, L. Trotochaud, A. M. Smith and S. W. Boettcher, *J. Am. Chem. Soc.*, **137**, 3638 (2015).
17. F. Cheng, J. Shen, W. Ji, Z. Tao and J. Chen, *ACS Appl. Mater. Interfaces*, **1**, 460 (2009).
18. W. Xiao, D. Wang and X. W. Lou, *J. Phys. Chem. C*, **114**, 1694 (2010).
19. Y. Gorlin, C.-J. Chung, D. Nordlund, B. M. Clemens and T. F. Jaramillo, *ACS Catal.*, **2**, 2687 (2012).
20. F. Jiao and H. Frei, *Chem. Commun.*, **46**, 2920 (2010).
21. S. Chen, T. Zhai, X.-H. Lu, M.-Z. Zhang, Z.-Y. Li, C.-W. Xu and Y. Tong, *Int. J. Hydrogen Energy*, **37**, 13350 (2012).
22. Y. Xu, H. Jiang, X. Li, H. Xiao, W. Xiao and T. Wu, *J. Mater. Chem. A*, **2**, 13345 (2014).
23. H.-Y. Su, Y. Gorlin, I. C. Man, F. Calle-Vallejo, J. K. Nørskov, T. F. Jaramillo and J. Rossmeisl, *Phys. Chem. Chem. Phys.*, **14**, 14010 (2012).
24. H. Duan, N. Yan, R. Yu, C.-R. Chang, G. Zhou, H.-S. Hu, H. Rong, Z. Niu, J. Mao, H. Asakura, T. Tanaka, P. J. Dyson, J. Li and Y. Li, *Nat. Commun.*, **5**, 3093 (2014).
25. C. Koenigsmann, D. B. Semple, E. Sutter, S. E. Tobierre and S. S. Wong, *ACS Appl. Mater. Interfaces*, **5**, 5518 (2013).
26. Y. Yan, B. Xia, X. Ge, Z. Liu, J.-Y. Wang and X. Wang, *ACS Appl. Mater. Interfaces*, **5**, 12794 (2013).
27. H. Zhang, Z. Ma, J. Duan, H. Liu, G. Liu, T. Wang, K. Chang, M. Li, L. Shi, X. Meng, K. Wu and J. Ye, *ACS Nano*, **10**, 684 (2016).
28. L. Liu, Z. Yang, H. Liang, H. Yang and Y. Yang, *Mater. Lett.*, **61**, 891 (2010).
29. Y. Sun, X. Hu, W. Luo and Y. Huang, *J. Mater. Chem.*, **22**, 19190 (2012).
30. Y. Zhang, Y. Yan, X. Wang, G. Li, D. Deng, L. Jiang, C. Shu and C. Wang, *Chem. Eur. J.*, **20**, 6126 (2014).
31. S.-Z. Huang, Y. Cai, J. Jin, J. Liu, Y. Li, Y. Yu, H.-E. Wang, L.-H. Chen and B.-L. Su, *Nano Energy*, **12**, 833 (2015).
32. K. Ramesh, L. Chen, F. Chen, Y. Liu, Z. Wang and Y.-F. Han, *Catal. Today*, **131**, 477 (2008).
33. B. Liu, X. Hu, H. Xu, W. Luo, Y. Sun and Y. Huang, *Sci. Rep.*, **4**, 4229 (2014).
34. N. D. Petkovich and A. Stein, *Chem. Soc. Rev.*, **42**, 3721 (2013).
35. X.-Y. Yang, L.-H. Chen, Y. Li, J. C. Rooke, C. Sanchez and B.-L. Su, *Chem. Soc. Rev.*, **46**, 481 (2017).
36. Y. Fang, Y. Huang, S. Zhang, W. Jia, X. Wang, Y. Guo, D. Jia and L. Wang, *Chem. Eng. J.*, **315**, 583 (2017).
37. A. Ramírez, P. Hillebrand, D. Stellmach, M. M. May, P. Bogdanoff and S. Fiechter, *J. Phys. Chem. C*, **118**, 14073 (2014).
38. D. P. Dubal, D. S. Dhawale, R. R. Salunkhe, V. J. Fulari and C. D. Lokhande, *J. Alloys Compd.*, **497**, 166 (2010).
39. G. Liu, X. Gao, K. Wang, D. He and J. Li, *Nano Res.*, **10**, 2096 (2017).